Energy 132 (2017) 315–323

Contents lists available at ScienceDirect

Energy

journal homepage: www.elsevier.com/locate/energy

Dynamic Paths: Towards high frequency direct normal irradiance forecasts

Carlos M. Fernández Peruchena [a, *], Martín Gastón [b], Marion Schroedter-Homscheidt [c], Miriam Kosmale [c], Isabel Martínez Marco [d], José Antonio García-Moya [d], José L. Casado-Rubio [d]

[a] National Renewable Energy Centre (CENER), C/ Isaac Newton n 4 - Pabellón de Italia, 41092, Seville, Spain
[b] CENER, Spain
[c] German Aerospace Center (DLR), Germany
[d] Agencia Estatal de Meteorología (AEMET), Spain

ARTICLE INFO

Article history:
Received 22 August 2016
Received in revised form
21 March 2017
Accepted 15 May 2017
Available online 16 May 2017

Keywords:
Forecast
Dynamic Path
High-frequency
Variability
DNI
Numerical weather prediction (NWP)

ABSTRACT

Direct normal solar irradiance (DNI) series of high-frequency time resolution permit an accurate modeling and analysis of transient processes in concentrating solar thermal power (CSTP) technologies. Numerical weather prediction (NWP) models provide an overall understanding of solar forecasting, but they are unlikely to cover a local statistical representativeness of the DNI high frequency dynamics. On the contrary, local statistical information derived from site measurements can provide statistical behavior, but may not necessarily yield an explicit model for all of the physical relationships involved. In this work, we propose a novel locally-adapted procedure for high-frequency DNI forecasting that connects these two extremes, proposing a hybrid approach in which low frequency (3-h) NWP outcomes act as boundary conditions (assuring a physical consistency with site climatic behavior) and are supplemented with Dynamic Paths of local high frequency (1-min) DNI series (assuring a statistical reproduction of site high frequency dynamics). This methodology is tested with ground measurements in 4 locations situated in different climates, and compared with a forecast base case. The analyses are carried out by classifying each measured time series into 6 categories according to its daily clearness index. Finally, metrics for adequately compare high frequency DNI forecasts are discussed.

1. Introduction

A detailed knowledge of the Direct Normal solar Irradiance (DNI) is a critical point in the design and management of a Concentrating Solar Thermal Power (CSTP) plant, since the DNI is the most determining variable in its final energy yield. High-frequency DNI series allow an accurate modeling and analysis of transient processes in some CSTP technologies, which show a nonlinear response to DNI governed by various thermal inertias owing to their complex response characteristics. DNI variability at high-frequency exerts substantial influence on the grid integration of electric power generation by CSTP technologies, which entails the necessity of developing forecasting methodologies for large-scale integration of these technologies into current energy supply structures [1,2].

Accurate DNI forecasting is of utmost importance for the optimal management of energy markets, operation of CSTP plants and for the power generation control by means of thermal energy storage (if available). This allows maintaining the grid stability in CSTP power management and ultimately facilitates the widespread implementation of CSTP technologies [3]. DNI forecasting method depends strongly on the timescale of interest, which ranges from horizons of a few seconds or minutes to several days-ahead. In the case of CSTP, the variability in irradiances is generally dampened in the electricity generation by the use of large thermal storages. Nevertheless, also CSTP plants are affected by variability of the DNI in their daily operations. For trough technologies, the second-wise or the 1-min-wise variability is not of concern, but the variability in the 10 min scale is relevant to describe transient effects [4]. On the other hand, in solar tower technologies, the high frequency on the minute scale is relevant as the thermal receiver may be damaged by

* Corresponding author.
E-mail address: cfernandez@cener.com (C.M. Fernández Peruchena).

http://dx.doi.org/10.1016/j.energy.2017.05.101

fast and large temperature gradients. In order to avoid such gradients, the heliostats are frequently defocused and such a control system requires information on variability in and below the 1-min scale [4]. For the intra-hour and intraday, it is common to use the conversion of cloud positioning as derived by sky cameras into solar radiation deterministic models [5,6]. For 1–2 h ahead horizons, solar irradiance is predicted with good accuracy by means of statistical approaches, including ARIMA (autoregressive integrated moving averages) and ANN (artificial neural network) [1,7–11]. For 2–6 h time horizons, cloud index derived from satellite images is used in cloud-motion vector schemes [12–15]. Numerical weather prediction (NWP) schemes are also used in connection to air quality models to provide forecasts taking aerosol variability into account [16–19]. Forecast models for the 1–5 days ahead have also been developed with good accuracy and reliability [1,20]. It is worth to highlight that the vast majority of conventional generation is scheduled in the day-ahead market [21].

Unfortunately, the solar irradiance forecast in NWP models has not been treated traditionally as a priority as it has been mainly used to force the average Earth's surface energy balance. This situation, influenced by the traditional lack of major stakeholders, is changing in recent years in which substantial investments are now being made in this field due to the increasing demand for operational and improved solar forecasts. In this regard, it is worth to mention verification efforts that have recently been undertaken with respect to hourly resolved DNI forecasts as provided by the European Centre for Medium-Range Weather Forecasts (ECMWF) [22]. Notwithstanding, it is clear that the industry demands higher temporal resolution forecasted DNI series that those achieved by NWP models, which typically ranges from 1 h to 3 h in global scale modeling. Also, a detailed site dynamic of high-frequency DNI is not provided by these models [23]. The high variability of atmospheric phenomena as clouds and aerosols, the complex atmospheric modeling on which NWP models rely, the extremely large underlying systems for data capture and assimilation and, in general, the large uncertainty associated with weather behavior makes accurate localized and high-frequency forecasting a very difficult task.

The variability of solar irradiance is strongly dependent on the local microclimate and the averaging timescale used [24–26]. Apart from the solar position (which is completely deterministic), the DNI variability is mostly due to clouds, which can be associated with a stochastic nature as precise models for cloud dynamics have proven elusive [27]. Aerosols also contribute to the DNI variability, but they cause variations on a several-hour time scale [28] while clouds affect DNI in the minute time scale: CSTP plants production changes can exceed 50% of the clear sky generation potential over two to 5 min [29]. Moreover, rapid changes in solar power output can impact markets with sub-hour intervals, reserve requirements, net load variability, regulation requirements, and the operation of other generators [30]. To capture these potentially challenging events in technology evaluation studies, high temporal resolution input DNI data are required.

In this work, we present a novel approach for statistical post-processing of 3-h DNI series that dynamically assembles site information to provide high frequency DNI series up to the temporal resolution of available measurements at the site. The 3-h temporal resolution is selected as a case study based on the ECMWF, which provides both global and direct irradiance forecasts commercially at this time resolution. The rationale for this data-driven approach is that patterns exist in the historical dataset that can be used for characterizing high frequency DNI dynamics at the site [31] together with a forecast of the DNI values at clearest sky conditions. This novel approach is compared with a base case, consisting in the linear interpolation of clear sky condition each 3-h throughout the day.

The paper is presented as follows: Section 2 describes measured data used in the work, as well as the analysis carried out. Section 3 shows the results found and in Section 4 discussion, conclusions and future work are drawn.

2. Methods

2.1. Ground-measured observations

For this study, we have selected high quality solar irradiance data from the Baseline Surface Radiation Network (BSRN) stations [32] located at Carpentras (CAR), Lauder (LAU), Sede Boquer (SBO), and Tamanrasset (TAM). Table 1 shows details about the locations of the stations selected for this study, as well as their climatic conditions according to the Köppen–Geiger classification [33]. This climatic scheme divides the climate in five main types and several subtypes, mainly based on mean temperature and precipitation values. A further characterization of the stations CAR, SBO, and TAM is provided by making use of variability classes as suggested by Ref. [34]. Fig. 1 provides frequency histograms of the occurrence of each variability class in the time series from 2005 to 2011 in CAR and SBO (left), and from 2008 to 2014 in TAM (right). LAU location is excluded from this analysis because the classification scheme has been developed and tested also with satellite data, and is therefore available only for the Meteosat Second Generation field of view.

The most frequent case in CAR location is the variability class 8

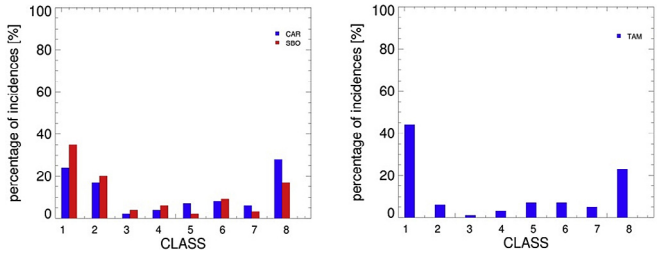

Fig. 1. Frequency histogram of variability classification results for BSRN stations CAR, SBO, and TAM based on daytime hours in the years 2005–2011 (for CAR and SBO, left) and 2008–2014 (in the case of TAM, right).

Table 1
Radiometric stations selected for this study.

Location (ID)	Country	Coordinates	Altitude (m)	years	Climate following Köppen and Geiger
Carpentras (CAR)	France	44.0830 N 5.0590 E	100	2005–2011	Mediterranean
Sede Boquer (SBO)	Israel	30.8597 N 34.7794 E	500	2005–2011	Hot desert, arid
Tamanrasset (TAM)	Algeria	22.7903 N 5.5292 E	1385	2008–2014	Hot desert, arid
Lauder (LAU)	New Zealand	45.0450 S 169.6890 E	350	2008–2014	Oceanic

which shows a percentage (28%) close to the second most frequent case (variability class 1, 25%). The third most frequent case is variability class 2 (17%). It is worth mentioning that variability class 8 is characterized by cloudy conditions (with little variability). On the opposite, variability class 1 is characterized by clear sky conditions without any variability and variability class 2 is characterized by small variability (i.e., few passing optically thin clouds). This pattern is consistent with a Mediterranean climate, where clear skies in summer coexist with cyclones with their attendant precipitation when the anticyclone moves Equator-ward in winter.

In the opposite scenario, TAM location shows a marked prevalence of variability class 1 (45%), which almost doubles the percentage of the second most frequent case (variability class 8, 23%). This result is congruent with the fact that TAM location belongs to a desert climate, with a high percentage of cloud-free conditions throughout the year. Dominant high pressure and lack of moisture combine to inhibit the production of clouds.

Conversely, SBO location shows an intermediate behavior between CAR and TAM locations. Even if it shows a prevalence of variability class 1 (35%) as observed in TAM location, its second most frequent case is variability class 2 (20%). This distribution of cases among variability classes 1 and 2 is more similar to the pattern as observed at CAR. Thus, variability classes found in SBO location are consistent with a desert climate, but it shows more passing clouds than the TAM location - especially in the highly variable classes 4 and 6 and in the low variability, but also low DNI class 8.

Global Horizontal solar Irradiance (GHI) datasets in CAR and LAU stations were collected by Kipp & Zonen CM21 and CM11 pyranometers respectively. GHI datasets in SBO TAM stations were collected by Eppley PSP Pyranometers. DNI datasets in CAR and LAU stations were collected by Kipp & Zonen CH1 and CHP1 Pyrheliometers respectively. DNI datasets in SBO and TAM stations were collected by Eppley NIP Pyrheliometers. The measurement period selected for each station corresponds to seven consecutive years. Station maintenance and instrument calibration, as well as and data quality control, are performed by the person in charge of the measurements to assure high accuracy as well as homogeneity in the data [32]. Also, the quality of the data was verified by the authors through a completeness of data analysis followed by a visual examination of the time series, and a subsequent quality control test based on principles of physical limits, likelihood of occurrence and concurrent trends on visually-validated measurement data.

The period used for characterizing the local high-frequency DNI patterns was the first two years of the datasets: 2005–2006 for CAR and SBO datasets; and 2008–2009 for TAM and LAU datasets.

2.2. Methods for increasing the temporal resolution of DNI series

An increase in resolution from 3-h DNI series as input to 1-min DNI series is performed through the following methodologies:

2.2.1. Linear interpolation (LI)

The path that solar radiation travels through the atmosphere is not a linear function of time. Consequently, a simple linear interpolation of DNI is inappropriate for increasing its temporal resolution. Persistence models are commonly used in forecast studies which typically assume that the ratio between the measured irradiance to the clear sky irradiance persists for the next time-step. In this work, a modification of this procedure is used: instead of persistence of this ratio, a linear interpolation of this parameter is carried out. While Schroedter-Homscheidt et al. [22] used this approach to generate an hourly out of three-hourly ECMWF resolved forecasts, this paper applies the approach to obtain 1-min resolved time series. Clear sky DNI values were calculated using the REST-2 model [35]. The LI procedure is used as base-case in this work.

2.2.2. Dynamic Paths (DP)

Instantaneous DNI exhibits a great variability at high-frequency due to the dynamic effects of passing clouds. To capture these potentially challenging events, the adimensionalization of measured high-frequency DNI curves is carried out both in the time and energy for each day:

- Measured DNI is divided by its corresponding clear sky DNI.
- Time elapsed since sunrise is divided by day length.

Clear-sky DNI profiles are calculated by appropriately adjusting the parameters of the clear-sky ASHRAE exponential model [36] so that the curve defined by the model is the tightest possible upper boundary of the cloudless measured DNI values for the given day [37–39]. The use of the ASHRAE model in this methodology does not intend to characterize a unique set of parameters for a given location, but the generation of a number of enveloping DNI curves in the location through the combination of those parameters.

Within this nondimensionalization scheme, every daily high-frequency DNI curve is transformed into a dimensionless curve where both the dimensionless time and irradiance scales goes from 0 to 1. Thus, high-frequency DNI describes Dynamic Paths in this non-dimensional space can be re-dimensioned for reproducing actual high-frequency DNI dynamics of each day (accordingly to clear-sky DNI profiles calculated for that particular day).

For increasing the temporal resolution of DNI series in a particular day, it is selected the combination of non-dimensional curves and daily clear sky DNI profiles that minimizes the root mean square error (RMSE) of input and generated 3-h DNI series. Also, only those generated daily DNI curves with a maximum DNI value within ±10% of the actual DNI value under clearest sky conditions are considered, to avoid the selection of those generated days not consistent with the forecasted atmospheric conditions. This step ties the statistical post-processing to the physical boundaries as provided by the NWP-based day ahead forecasted DNI for the specific day. The rationale for this data-driven approach is the characterization of both solar irradiance patterns existing in the historical dataset [31] and site-specific DNI daily profiles [37].

2.3. Time series verification metrics

Classical statistical metrics as RMSE or correlation coefficients are not suitable to evaluate the high frequency series generated by the method proposed in this work. It is not aimed at reproducing each single 1-min value of the ground measured time series exactly at the point in time, but its high-frequency dynamics throughout the day (in particular, variability and distributions). In this work, statistical parameters for comparing daytime (from sunrise to sunset) DNI measured and modeled series are calculated as a function of day type and location. The statistical metric used to check the distribution similitude between generated and measured high-frequency DNI values is the KSI (Kolmogorov-Smirnov test Integral) index, which is defined as the integrated differences between the Cumulative Distribution Functions (CDF) of two datasets [40].

A day-wise classification has been carried out in order to group measured DNI into different categories according to their daily clearness index, kt. The clearness index is defined as the ratio of Global Horizontal solar Irradiance (GHI) to the extraterrestrial solar irradiance on the same plane. All data are classified in the following daily kt intervals: (<0.3; 0.3–0.4; 0.4–0.5; 0.5–0.6; 0.6–0.7; >0.7), which are assigned to the following nominal values: <0.30; 0.35;

0.45; 0.55; 0.65; >0.70.

For quantifying solar variability from minute to minute, we use the following definition of ramp-rate (RR), adapted from the corresponding definition for GHI provided by Lave and Kleissl [41]:

$$RR = \frac{DNI(t) - DNI^{CS}(t) - [DNI(t-1) - DNI^{CS}(t-1)]}{\Delta t} \quad (1)$$

DNI irradiance under clear sky conditions, DNI^{CS}, is calculated using REST2 model [35] and is subtracted from the measured and generated DNI, such that the remaining value is the residual of the expected clear sky irradiance. Thus, the RR of these variations is calculated as the difference between successive data points from minute to minute DNI and in units of W/(m^2min).

For RR characterization, the absolute mean, standard deviation, skewness and kurtosis are calculated. Absolute mean and standard deviation characterizes, respectively, both the average and dispersion of datasets. Skewness is a measure of the degree of asymmetry of a distribution, and kurtosis is a measure of the combined weight of the tails relative to the rest of the distribution.

3. Results

It is obvious that DNI dynamics under clear sky conditions is highly predictable, as in this case atmospheric attenuating components change slowly. In the opposite scenario, under completely overcast sky conditions, DNI is zero. In these extreme cases, even simple forecast models can yield very good performance, becoming the transient cloud conditions the most unpredictable situations for these models. As different locations show in general different percentage of clear and cloudy days (Fig. 2, left), and also given the fact that high frequency solar irradiance is highly dependent on site [24] (Fig. 2, right), it is reasonable to break down the analysis into locations and day clearness index.

Table 2 shows, for the locations analyzed, the number of days included in each category defined in section 2.3 according to their daily kt (n), as well as their daily kt mean values (MV) and standard deviations (SD). As expected, a desert location (TAM) has the higher percentage of clearest days (daily kt > 0.70). It is worth to highlight the balance between day classes in LAU, and also the low atmospheric turbidity conditions in clearer days of TAM. Finally, the ratio of standard deviation to mean value of daily kt monotonically decreases with increasing mean daily kt classes, indicating lower dispersion at clearer conditions.

Fig. 3 shows measured DNI (red line, top) for several day classes in TAM station as well as the DNI values generated through the LI (middle line, green) and DP (bottom line, blue) procedures. The cloudiest measured day shown in the left part of Fig. 3 (daily kt = 0.35, 2013/05/06) has DNI peaks over 600 W/m^2, and rapid transitions between clear and cloud conditions prevailing the latter. This dynamic is well represented by the DP-generated DNI curve, which reproduces those rapid transitions, though with a slightly higher frequently. On the contrary, LI-generated DNI curves does not reach too high or zero values, keeping low values and smoothly increasing when DNI peaks measured are more frequently (and consequently, its 3-h averages increases).

It is worth to highlight that, for this day, RMSE between measured and generated series is lower for LI (117 W/m^2) than for DP procedure (178 W/m^2). This fact is due to the high differences found between DP-generated and measured DNI values: peaks in these datasets are not simultaneously, but they can alternate increasing considerably RMSE values. On the contrary, LI-generated DNI series shows a smooth dynamics, passing their values through the measured DNI peaks and minimizing the root square of their differences. With respect to their distributions, DP-generated series has lower KSI (23%) than LI-generated series (275%).

Measured DNI series of days with daily kt of 0.45 and 0.55 shown in Fig. 3 (corresponding to 2011/05/31 and 2011/01/19, respectively) shows a flickering behavior, with a higher prevalence of clear sky conditions. In these cases, DP-generated series provide again a similar dynamic behavior than measured ones, by generating both peak amplitude and duration similar to those observed.

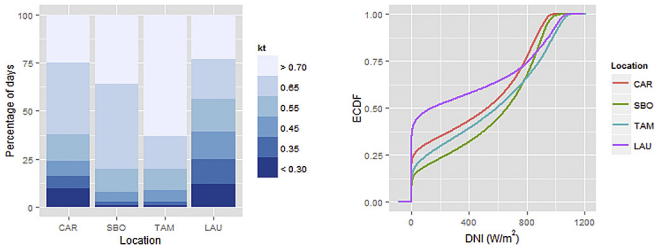

Fig. 2. Left, percentage of type of days according to their clearness index; Right, empirical cumulative distribution functions of DNI.

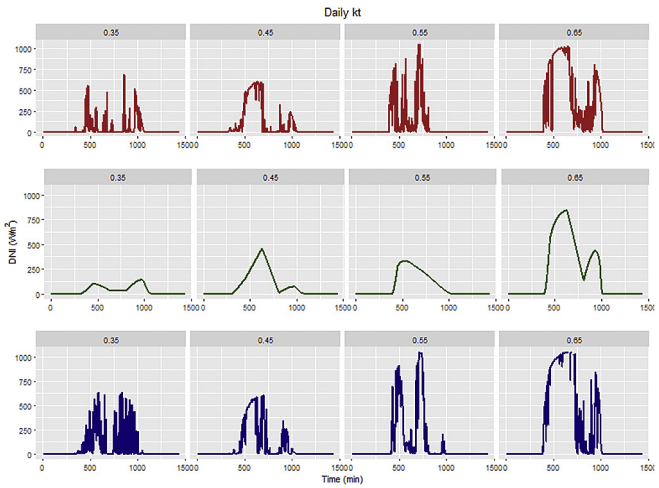

Fig. 3. Measured (top), LI (middle) and DP (bottom) generated DNI at TAM, for different day types.

Table 2
Statistical information for daily kt intervals in each location analyzed.

Daily kt interval	Assigned nominal value	CAR			SBO			TAM			LAU		
		n	MV	SD	n	MV	SD	n	MV	SD	n	MV	SD
0.0–0.3	<0.30	155	0.219	0.059	20	0.241	0.042	6	0.236	0.056	163	0.234	0.052
0.3–0.4	0.35	104	0.347	0.031	31	0.357	0.029	22	0.362	0.027	178	0.350	0.027
0.4–0.5	0.45	136	0.455	0.030	78	0.456	0.030	63	0.462	0.026	189	0.452	0.028
0.5–0.6	0.55	224	0.553	0.029	205	0.558	0.028	119	0.556	0.027	223	0.554	0.03
0.6–0.7	0.65	586	0.660	0.027	745	0.663	0.026	178	0.651	0.028	288	0.651	0.028
0.7–1.0	>0.70	397	0.723	0.014	604	0.727	0.017	651	0.768	0.031	310	0.742	0.026

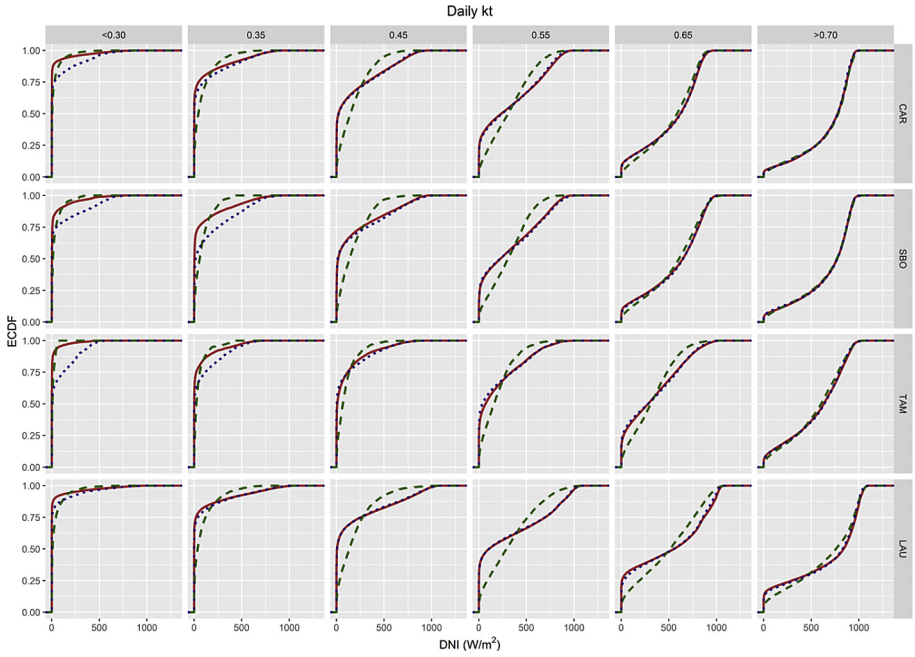

Fig. 4. ECDF of measured (red continuous lines) and generated (DP, blue dotted lines; LI, green dashed lines) DNI series.

RMSE between measured and generated series is greater in the DP-generated (135 W/m^2 and 296 W/m^2, respectively) than in LI-generated series (123 W/m^{2}and 271 W/m^2, respectively).

In the clearest day shown in Fig. 3 (daily kt = 0.65, corresponding to 2011/12/27), it is worth to mention a better performance of LI procedure in comparison with previous cases, which roughly follows the peak dynamics in measured DNI series. The DP-generated series also faithfully reproduce peak amplitude and duration of measured series in this case. RMSE between measured and generated series is again lower in the LI (244 W/m^2) than in DP series (267 W/m^2). Finally, KSI values keep lower in these DP-generated series (5%, 6% and 14% for daily kt of 0.45, 0.55 and 0.65 respectively) than in the corresponding LI-generated series (47%, 105% and 19%, for daily kt of 0.45, 0.55 and 0.65 respectively).

Having now discussed single days as examples, in the following statistical results are provided for the full time series period. Fig. 4 shows empirical cumulative distribution function (ECDF) of measured and generated DNI series for the locations and the daily kt intervals studied, where only daytime values are used in the analyses.

Measured 1-min DNI ECDF values (red continuous lines) in the daily kt < 0.30 category are located at the left part of the graph. These days are characterized by a high percentage of measured DNI values equal to zero (completely overcast conditions) and low maximum measured DNI values. At increasing daily kt values, there is a site-dependent smooth transition of the measured 1-min DNI curve: large DNI values occur more frequently, while the number of low DNI values decrease. LI ECDF (green dashed lines) differs from the measured one in intermediate kt days (0.45 and 0.55), while the DP ECDF (blue dotted lines) remains much closer to the measured ECDF. For very clear skies (daily kt ≥ 0.65), DP ECDF almost exactly fit the measured ones, while the LI ECDF become more similar to the measured ones (especially in the case kt > 0.70). This fact suggests a slow dynamics in the intraday evolution of the atmospheric turbidity under very clear skies, properly represented by a 3-h series (interpolated to 1-min).

Table 3 shows KSI values calculated from the comparison of generated and measured DNI series. DP-generated series keep always KSI values lower than LI ones, indicating their better similarity with measured distributions. In particular, intermediate day types (daily kt values of 0.45 and 0.55) are well reproduced by this procedure in all stations analyzed. It is worth to mention that these cases comprise days which normally have enough DNI for CSTP generation and also frequent passing clouds. As expected, KSI of the LI-generated is lower for extreme cases analyzed (daily kt < 0.30, and ≥0.65), where the most homogeneity sky situations are given.

Table 3
KSI (%) values obtained in the comparison of measured and generated 1-min DNI series.

Daily kt	CAR		SBO		TAM		LAU	
	LI	DP	LI	DP	LI	DP	LI	DP
<0.30	126.3	83.1	115.3	48.7	515.9	77.6	124.5	29.2
0.35	183.6	34.3	211.3	63.6	94.5	39.4	126.7	14.4
0.45	231.0	9.2	175.1	17.9	122.1	16.1	187.0	7.1
0.55	216.7	17.5	192.1	18.4	188.5	16.3	198.7	6.9
0.65	123.1	14.6	111.1	28.9	149.0	17.5	140.8	25.2
>0.70	16.3	8.9	21.3	15.8	51.0	14.2	60.2	15.3

LI-generated series have their lower KSI values (below 100%) at daily kt > 0.70, as expected (simplistic forecast algorithms can yield very good conventional statistical metrics). The better performance of DP procedure in these days is attributed to the flexibility that this methodology offers in reproducing unusual clear sky profiles, as well as the presence of rapid falls and rises in clear sky DNI profiles (Fig. 5, right, corresponding to 2008/07/14). At the other extreme, the worst KSI values in DP-generated series are found at daily kt < 0.30. These days are frequently not adequate for CSTP generation, and DNI dynamics is highly unpredictable mainly due to sparse DNI peaks with a wide variety of height and duration (Fig. 5, left, corresponding to 2010/01/07).

Fig. 6 (left) shows RR for daytime DNI measured in 2012/04/05 at TAM (daily kt = 0.45), and the corresponding LI (center) and DP (right) generated RR. The measured and generated DNI series in this day can be seen in Fig. 3. RR of LI series shows a flat behavior, reflecting the smooth trend shown in its corresponding DNI curve. On the contrary, RR of measured and DP-generated series have

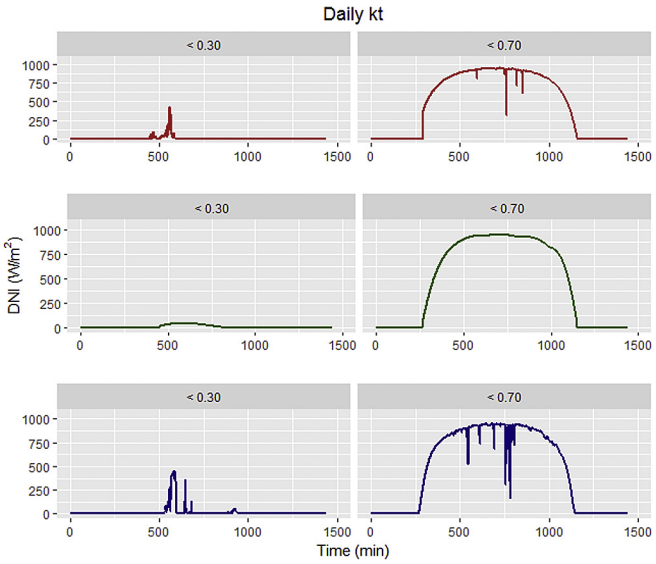

Fig. 5. Measured (top), LI (middle) and DP (bottom) generated DNI at CAR, for different day types.

multiple peaks with different amplitude, widths and duration, reflecting the variability of their corresponding DNI series (Fig. 3). Notwithstanding, these RR peaks are not coincident, neither in amplitude or location.

Absolute mean values and standard deviations of RRs are highly dependent on daily kt and location (Table 4), both in measured (*Me*) and generated series. Their highest values for measured data are usually found at intermediate daily kt cases (kt = 0.45 and 0.55), whereas the extreme day types (kt < 0.30 and kt > 0.70) show their lowest values reflecting more stable conditions. LI-RR absolute mean values and standard deviations keep low values (<2.2 W/(m^{2}min) and <5.4 W/(m^{2}min), respectively), whereas the values of these parameters in RR of DP-generated DNI series follows a similar trend to that observed in measured ones, but with lower values (in a factor of 0.83 and 0.76, respectively).

Table 5 shows kurtosis and skewness for DNI RR. Kurtosis characterizes the peakedness or flatness of a distribution compared to the normal distribution. All cases analyzed in this work have positive kurtosis (leptokurtic distribution), which reflects peaked distributions. Also, RR kurtosis analyzed in this work is highly dependent on daily kt and location. The highest kurtosis for measured DNI RR is found at extreme daily kt types (kt < 0.30 and kt > 0.70). In these cases, a great homogeneity of sky situations is given and most of RR values are grouped into a few range. These facts are associated with peaked distributions, and are also linked with the lower standard deviation of RR in these day categories. On the contrary, intermediate day types (in particular, kt = 0.45 and 0.55) have a greater variety of sky situations leading to flatter distributions. The kurtosis of measured and DP-generated RR has the same trend, being DP values lower (in a factor of 0.82 approximately). On the contrary, LI-generated RR has extremely high kurtosis values which are indicative of very sharp peaks.

Positively and negatively skewed distributions are asymmetric to the right and to the left respectively. In distributions asymmetric to the right, the tail on the right side of the peak is the longest one, and in distributions asymmetric to the left, the tail on the left side

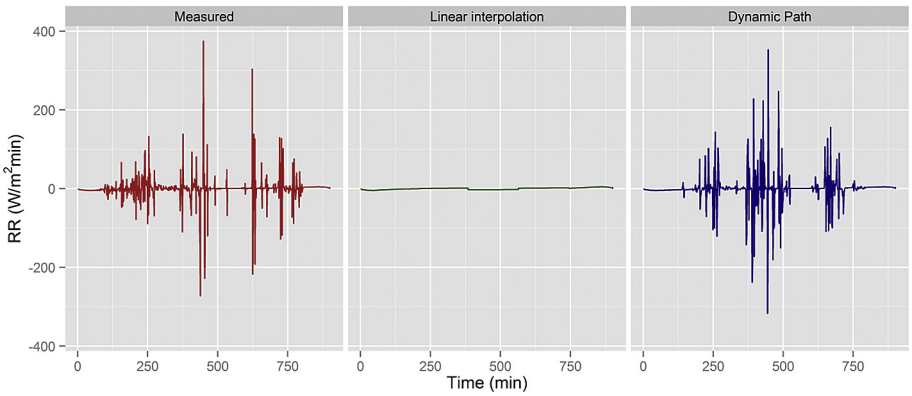

Fig. 6. Ramp rate of measured (left) and generated (LI, center; DP, right) in 2012/04/05 at TAM station (corresponding to a daily kt = 0.45).

Table 4
Ramp rate absolute mean and standard deviation for daytime measured and generated 1-min DNI series.

Parameter	Daily kt	CAR			SBO			TAM			LAU		
		Me	LI	DP	Me	LI	DP	Me	LI	DP	Me	LI	DP
Absolute mean W/(m^{2}min)	<0.30	10.1	2.0	10.9	12.4	2.1	17.1	10.7	2.2	10.8	11.5	1.9	12.6
	0.35	22.4	1.9	19.9	30.4	1.9	34.6	15.3	1.8	16.5	23.9	1.9	20.9
	0.45	35.9	1.9	26.4	45.9	1.9	31.8	22.0	1.8	18.9	37.4	2.0	30.5
	0.55	36.5	1.8	27.4	56.8	1.6	40.2	31.9	1.7	26.5	48.0	2.2	37.1
	0.65	21.9	1.1	14.1	25.8	1.2	15.9	39.5	1.4	26.7	44.3	2.0	30.5
	>0.70	11.0	1.0	6.4	11.0	0.9	7.9	18.7	1.0	11.5	28.6	1.5	18.3
SD W/(m^{2}min)	<0.30	39.6	4.2	34.4	42.4	3.7	49.0	34.7	5.4	27.8	48.3	4.2	40.7
	0.35	63.8	4.1	50.8	83.0	3.2	75.3	47.6	2.9	40.7	73.8	4.7	57.6
	0.45	84.0	5.5	59.7	109.4	4.5	74.6	55.2	3.4	48.6	95.9	4.9	73.8
	0.55	85.1	5.4	58.7	122.0	3.9	89.0	72.0	3.6	62.1	114.5	5.3	84.4
	0.65	63.5	4.6	39.0	80.3	4.3	49.2	87.5	3.6	59.2	112.3	5.2	74.2
	>0.70	40.8	3.8	24.0	44.0	3.8	30.2	57.5	3.5	36.3	87.6	4.5	53.0

Table 5
Ramp rate kurtosis and skewness for daytime measured and generated 1-min DNI series.

Parameter	Daily kt	CAR			SBO			TAM			LAU		
		Me	LI	DP	Me	LI	DP	Me	LI	DP	Me	LI	DP
Kurtosis (−)	<0.30	70.7	2171.4	42.0	54.6	368.4	22.4	42.7	794.2	24.2	72.9	1621.3	37.5
	0.35	28.8	1071.0	18.3	20.1	477.3	10.5	47.4	616.1	16.8	31.2	2373.3	22.9
	0.45	16.4	1878.7	16.2	13.6	889.0	12.9	24.0	701.5	21.4	18.5	2514.5	16.5
	0.55	18.3	1333.1	13.5	10.3	1366.1	9.5	15.4	1129.7	15.0	14.6	2266.4	12.3
	0.65	36.1	1615.1	34.1	29.0	1164.4	33.6	13.1	1462.5	13.1	16.2	1771.8	16.4
	>0.70	93.8	1281.7	102.8	79.4	972.4	70.6	37.8	1533.6	42.0	29.0	1072.8	26.5
Skewness W/(m^{2}min)	<0.30	−0.3	−15.5	−0.2	0.1	−1.4	−0.2	−0.8	−1.8	−0.5	−0.1	−17.2	0.1
	0.35	−0.1	−7.4	−0.1	−0.1	4.0	−0.1	0.1	11.2	−0.1	0.2	−24.8	0.1
	0.45	0.1	6.6	−0.2	−0.1	5.8	0.1	−0.1	−4.7	−0.2	0.0	−11.1	0.2
	0.55	−0.1	5.5	0.0	0.0	8.2	0.0	−0.1	−2.0	−0.3	0.0	−16.3	0.1
	0.65	0.0	−4.0	0.1	0.0	9.0	0.1	0.0	−12.0	−0.1	0.0	−12.1	0.0
	>0.70	0.1	6.4	0.7	0.5	−23.7	0.3	0.0	−1.3	0.0	0.0	−18.2	0.0

of the peak is the longest. RR of measured and DP-generated DNI series keep low skewness values (lower than 1 W/(m^{2}min) in absolute value), which is indicative of symmetry in these data distributions. Conversely, RR of LI-generated DNI series shows high negative and positive skewness values, from 11.2 W/(m^{2}min) to 24.8 W/(m^{2}min).

4. Conclusions

Limitations in spatial and temporal resolution, as well as complexity in cloud microphysics and their radiative properties, makes it difficult to accurately predict DNI with NWP models at high temporal resolution. Hence, NWP models provide at best an overall and low frequency understanding of solar forecasting (typically 1 h–3 h in global scale modeling), but they are unable to cover a local statistical representativeness of the DNI high frequency dynamics. Unfortunately, the use of low frequency DNI series filters out their shorter time-scale intermittencies and hence hinders the management and integration of power output from CSTP plants. On the other hand, purely stochastic methods (in which there is no physical model per se but nonlinear interactions between variables) cover statistical behavior but may not necessarily yield an explicit model for all of the physical relationships involved.

One possible way to overcome the weaknesses of individual methods is to develop hybrid methodologies that capitalize on the strengths of both approaches, so that the end result is a forecasting system that is robust, flexible, and accurate [27]. In this context, this work explores a methodology that connects these two extremes, proposing a hybrid approach in which the following inputs are supplemented:

- Low frequency (3-h) DNI series representative of site climate
- Dynamic Paths of local high frequency DNI series

The results are analyzed in several locations with different climates and classified according to the day type (from cloudy to clear sky conditions), and also compared with a base-case consisting in the linear interpolation of sky conditions calculated at 3-h intervals.

The wide variety of high frequency solar irradiance transitions at different solar elevations, day types, hourly averages, its autocorrelation [42,43] and also its site-dependency [24], makes it unaffordable to exactly predict minute-to-minute DNI transitions at a given location. Consequently, we have characterized high frequency DNI behavior through non-dimensional dynamic patterns (instead minute-to-minute DNI transitions) in order to generate DNI series which are statistically indistinguishable to those measured (in terms of distribution and variability).

In evaluating solar irradiance forecasts, it is necessary to clearly define conditions so that different forecast models can be properly compared [44]. The findings of this work suggest not using RMSE (or similar indicators of dispersion) for evaluating high frequency DNI forecasts but focus on solar irradiance fluctuations amplitude, persistence, and frequency of occurrence rather than their location in time as well as their distribution. This high frequency characterization must be coupled with lower frequency solar irradiance dynamics provided by NWP models that acting as boundary conditions assure a physical consistency with site climate behavior. This work addresses this issue by proposing the site differentiation (so that local DNI patterns are investigated independently) and also by analyzing the time series on different temporal resolutions and with specific metrics. KSI index is used for the full length of the time series. Day types according to their clearness index are differentiated so that clear or cloud dominated days are treated separately. Overall, a better representation of the variability of 1-min DNI in the Dynamic Path approach has been found in these metrics compared to the linear interpolation of the clear sky index used as base case.

In this work, only 3-h DNI averages and maximum clear-sky DNI values (with ±10% accuracy) are used as inputs to generate the DNI series by the Dynamic Path procedure. Future improvements will include the blend of a wide variety of inputs of different nature to optimally select Dynamic Paths in the generation, as meteorological information and cloud predictions provided by NWP models, satellite or sky camera images (for short term forecast). Moreover, hourly frequency solar irradiance intervals can be classified according to their averaged air masses and solar irradiation [24], as well as other parameters, in order to be associated with specific high frequency Dynamic Paths for coupling different time scales in the solar resource assessment and forecast. This would allow the association of Dynamic Paths in an hour with generic *variability classes* [34,45]. It is worth also to mention that recent works suggest that this procedure can be also adapted for high frequency GHI forecasts [46].

Finally, in the ground-measured observations description (Section 2.1) we found that SBO location shows more passing clouds (under mostly clear sky conditions) than TAM location. This difference, which may have implications in CSTP design and management, are not appreciated either in their climate zones (both belongs to hot desert climate) or in their annual DNI averages (2459 and 2419 kWh/m^2, respectively, according to [47]). This fact is indicative of the importance of local distribution and type of clouds in solar irradiance distributions, and highlight the role of local atmospheric clear sky transparency in differentiating these distributions, as described in Ref. [24]. These results point to the necessity of characterize locations in a more depth way than just

with annual irradiation (and even climate zone) for pre-feasibility studies. In this context, the variability classes may represent an effective approach for providing complementary information to the commonly used information in these studies if they are linked to specific high-frequency solar irradiance distributions [24].

Acknowledgements

This project has received funding from the European Union's Horizon 2020 research and innovation programme in the Pre-FlexMS project under grant agreement No 654984. The authors would like also to thank the manager and staff of Carpentras, Sede Boquer, Tamanrasset and Lauder BSRN stations for their efforts in establishing and maintaining that stations.

References

[1] Marquez R, Coimbra CFM. Forecasting of global and direct solar irradiance using stochastic learning methods, ground experiments and the NWS database. Sol Energy 2011;85:746–56. http://dx.doi.org/10.1016/j.solener.2011.01.007.
[2] Rodriguez GD. A utility perspective of the role of energy storage in the smart grid. IEEE PES Gen Meet 2010:1–2. http://dx.doi.org/10.1109/PES.2010.5589870.
[3] Mathiesen P, Kleissl J. Evaluation of numerical weather prediction for intra-day solar forecasting in the continental United States. Sol Energy 2011;85:967–77. http://dx.doi.org/10.1016/j.solener.2011.02.013.
[4] Hirsch T, Martin Chivelet N, Gonzalez Martines L, Biencinto Murga M, Wilbert S, Schroedter-Homscheidt M, et al. Technical report on the functional requirements for the nowcasting method. Deliverable 2.1 in the Direct Normal Irradiance Nowcasting methods for optimized operation of concentrating solar technologies (DNICast) project. 2014. available on, http://www.dnicast-project.net/en/index.php.
[5] Chow CW, Urquhart B, Lave M, Dominguez A, Kleissl J, Shields J, et al. Intra-hour forecasting with a total sky imager at the UC San Diego solar energy testbed. Sol Energy 2011;85:2881–93. http://dx.doi.org/10.1016/j.solener.2011.08.025.
[6] Marquez R, Coimbra CFM. Intra-hour DNI forecasting based on cloud tracking image analysis. Sol Energy 2013;91:327–36. http://dx.doi.org/10.1016/j.solener.2012.09.018.
[7] Cao J, Lin X. Study of hourly and daily solar irradiation forecast using diagonal recurrent wavelet neural networks. Energy Convers Manag 2008;49:1396–406. http://dx.doi.org/10.1016/j.enconman.2007.12.030.
[8] Paoli C, Voyant C, Muselli M, Nivet M-L. Forecasting of preprocessed daily solar radiation time series using neural networks. Sol Energy 2010;84:2146–60. http://dx.doi.org/10.1016/j.solener.2010.08.011.
[9] Pedro HTC, Coimbra CFM. Assessment of forecasting techniques for solar power production with no exogenous inputs. Sol Energy 2012;86:2017–28. http://dx.doi.org/10.1016/j.solener.2012.04.004.
[10] Reikard G. Predicting solar radiation at high resolutions: a comparison of time series forecasts. Sol Energy 2009;83:342–9. http://dx.doi.org/10.1016/j.solener.2008.08.007.
[11] Sfetsos A, Coonick AH. Univariate and multivariate forecasting of hourly solar radiation with artificial intelligence techniques. Sol Energy 2000;68:169–78. http://dx.doi.org/10.1016/S0038-092X(99)00064-X.
[12] Hammer A, Heinemann D, Hoyer C, Kuhlemann R, Lorenz E, Müller R, et al. Solar energy assessment using remote sensing technologies. Remote Sens Environ 2003;86:423–32. http://dx.doi.org/10.1016/S0034-4257(03)00083-X.
[13] Hammer A, Heinemann D, Lorenz E, Lückehe B. Short-term forecasting of solar radiation: a statistical approach using satellite data. Sol Energy 1999;67:139–50. http://dx.doi.org/10.1016/S0038-092X(00)00038-4.
[14] Lorenz E, Hurka J, Heinemann D, Beyer HG. Irradiance forecasting for the power prediction of grid-connected photovoltaic systems. IEEE J Sel Top Appl Earth Obs Remote Sens 2009;(2):2–10. http://dx.doi.org/10.1109/JSTARS.2009.2020300.
[15] Schroedter-Homscheidt M, Pulvermüller B. Verification of direct normal irradiance foreasts for the concentrating solar thermal power plant Andasol-3 location. In: SolarPACES conf. Proc., Granada (Spain); 2011. Paper id: 23213.
[16] Breitkreuz H, Schroedter-Homscheidt M, Holzer-Popp T. A case study to prepare for the utilization of aerosol forecasts in solar energy industries. Sol Energy 2007;81:1377–85. http://dx.doi.org/10.1016/j.solener.2007.01.009.
[17] Breitkreuz H, Schroedter-Homscheidt M, Holzer-Popp T. Dech S. Short-Range Direct and Diffuse Irradiance Forecasts for solar energy applications based on aerosol chemical transport and numerical weather modeling. J Appl Meteorol Climatol 2009;48:1766–79. http://dx.doi.org/10.1175/2009JAMC2090.1.
[18] Wittmann M, Breitkreuz H, Schroedter-Homscheidt M, Eck M. Case studies on the use of solar irradiance forecast for optimized operation strategies of solar thermal power plants. IEEE J Sel Top Appl Earth Obs Remote Sens 2008;(1):18–27. http://dx.doi.org/10.1109/JSTARS.2008.2001152.
[19] Schroedter-Homscheidt M, Oumbe A, Benedetti A, Morcrette J-J. Aerosols for concentrating solar electricity production forecasts: requirement quantification and ECMWF/MACC aerosol forecast assessment. Bull Am Meteorol Soc 2013;94:903–14. http://dx.doi.org/10.1175/BAMS-D-11-00259.1.
[20] Perez R, Kivalov S, Schlemmer J, Hemker Jr K, Renné D, Hoff TE. Validation of short and medium term operational solar radiation forecasts in the US. Sol Energy 2010;84:2161–72. http://dx.doi.org/10.1016/j.solener.2010.08.014.
[21] Kleissl J. Solar energy forecasting and resource assessment. Academic Press; 2013.
[22] Schroedter-Homscheidt M, Benedetti A, Killius N. Verification of ECMWF and ECMWF/MACC's global and direct irradiance forecasts with respect to solar electricity production forecasts. Meteorol Z 2017;26:1–19.
[23] Göber M, Zsótér E, Richardson DS. Could a perfect model ever satisfy a naïve forecaster? On grid box mean versus point verification. Meteorol Appl 2008;15:359–65.
[24] Fernández-Peruchena CM, Bernardos A. A comparison of one-minute probability density distributions of global horizontal solar irradiance conditioned to the optical air mass and hourly averages in different climate zones. Sol Energy 2015;112:425–36. http://dx.doi.org/10.1016/j.solener.2014.11.030.
[25] Fernández Peruchena CM, Ramírez L, Silva-Pérez MA, Lara V, Bermejo D, Gastón M, et al. A statistical characterization of the long-term solar resource: towards risk assessment for solar power projects. Sol Energy 2016;123:29–39. http://dx.doi.org/10.1016/j.solener.2015.10.051.
[26] Fernández-Peruchena CM, Gastón M, Sánchez M, García-Barberena J, Blanco M, Bernardos A. MUS: A multiscale stochastic model for generating plausible meteorological years designed for multiyear solar energy yield simulations. Sol Energy 2015;120:244–56. http://dx.doi.org/10.1016/j.solener.2015.07.037.
[27] Coimbra CFM, Kleissl J, Marquez R. Chapter 8-overview of solar-forecasting methods and a metric for accuracy evaluation. Sol. Energy Forecast. Resour. Assess. Boston: Academic Press; 2013. p. 171–94.
[28] Schepanski K, Klüser L, Heinold B, Tegen I. Spatial and temporal correlation length as a measure for the stationarity of atmospheric dust aerosol distribution. Atmos Environ 2015;122:10–21. http://dx.doi.org/10.1016/j.atmosenv.2015.09.034.
[29] Hummon M, Ibanez E. Brinkman, gregory, lew, debra. Sub-hour solar data for power system modeling from static spatial variability analysis. Lisbon, Portugal: National Renewable Energy Laboratory; 2012.
[30] Helman U, Loutan C, Rosenblum G, Guo T, Toolson E, Hobbs B. Integration of renewable resources: updated analysis of operational requirements and assessment of generation fleet capability under a 20% RPS requirement. IEEE PES Gen Meet 2010:1–2. http://dx.doi.org/10.1109/PES.2010.5590171.
[31] Wey E, Thomas C, Blanc P, Espinar B, Mouadine M, Bouhamidi M, et al. A fusion method for creating sub-hourly DNI-based TMY from long-term satellite-based and short-term ground-based irradiation data. In: Solar-PACES conf. Proc., Marrakech (Morocco); 2012. p. 693.
[32] Ohmura A, Gilgen H, Hegner H, Müller G, Wild M, Dutton EG, et al. Baseline surface radiation network (BSRN/WCRP): new precision radiometry for climate research. Bull Am Meteorol Soc 1998;79. http://dx.doi.org/10.1175/1520-0477(1998)079<2115:BSRNBW>2.0.CO;2. 2115–2136.
[33] Peel MC, Finlayson BL, McMahon TA. Updated world map of the Köppen-Geiger climate classification. Hydrol Earth Syst Sci 2007;11:1633–44. http://dx.doi.org/10.5194/hess-11-1633-2007.
[34] Schroedter-Homscheidt M, Jung S, Kosmale M. Classifying 1 minute temporal variability in global and direct normal irradiances within each hour from ground-based measurements. In: SolarPACES conf. Proc., Abu Dhabi (United Arab Emirates); 2016.
[35] Gueymard CA. REST2: high-performance solar radiation model for cloudless-sky irradiance, illuminance, and photosynthetically active radiation – validation with a benchmark dataset. Sol Energy 2008;82:272–85. http://dx.doi.org/10.1016/j.solener.2007.04.008.
[36] MacPhee C. ASHRAE handbook of fundamentals. New York: American Society of Heating; 1972. Refrigerating and Air Conditioning Engineers.
[37] Peruchena CMF, Blanco M, Bernardos A. Generation of series of high frequency DNI years consistent with annual and monthly long-term averages using measured DNI data. Energy Procedia 2014;49:2321–9. http://dx.doi.org/10.1016/j.egypro.2014.03.246.
[38] Fernández-Peruchena CM, Blanco M, Gastón M, Bernardos A. Increasing the temporal resolution of direct normal solar irradiance series in different climatic zones. Sol Energy 2015;115:255–63. http://dx.doi.org/10.1016/j.solener.2015.02.017.
[39] Fernández-Peruchena C, Blanco M, Bernardos A. Increasing the temporal resolution of direct normal solar irradiance series in a desert location. Energy Procedia 2015;69:1981–8. http://dx.doi.org/10.1016/j.egypro.2015.03.199.
[40] Espinar B, Ramírez L, Drews A, Beyer HG, Zarzalejo LF, Polo J, et al. Analysis of different comparison parameters applied to solar radiation data from satellite and German radiometric stations. Sol Energy 2009;83:118–25. http://dx.doi.org/10.1016/j.solener.2008.07.009.
[41] Lave M, Kleissl J. Solar variability of four sites across the state of Colorado. Renew Energy 2010;35:2867–73. http://dx.doi.org/10.1016/j.renene.2010.05.013.
[42] Beyer H-G, Fauter M, Schumann K, Schenk H, Meyer R. Synthesis of DNI time series with sub-hourly time resolution. In: SolarPACES conf. Proc., Perpignan (France); 2010. p. 55.
[43] Tomson T, Hansen M. Fast changes of the solar irradiance. Est J Eng 2010;16:

176–83.
[44] Kostylev V, Pavlovski A. Solar power forecasting performance – towards industry standards. In: 1st International Workshop on the Integration of Solar Power into Power Systems, Aarhus (Denmark); 2011.
[45] Jung S. Variabilität der solaren Einstrahlung in 1-Minuten aufgelösten Strahlungszeitserien. masters. Universität Augsburg; 2015.
[46] Fernández-Peruchena CM, Gastón M. A simple and efficient procedure for increasing the temporal resolution of global horizontal solar irradiance series. Renew Energy 2016;86:375–83. http://dx.doi.org/10.1016/j.renene.2015.08.004.
[47] Global Solar Atlas n.d. http://globalsolaratlas.info/(Accessed 08 March 2017).